

Aerodynamic Optimization of Flying-V Aircraft

Rasam R.S. Yazdi*, Thomas A. Reist†, and David W. Zingg‡

Institute for Aerospace Studies, University of Toronto, 4925 Dufferin St, Toronto, Ontario, M3H 5T6, Canada

High-fidelity aerodynamic optimization based on the Reynolds-averaged Navier-Stokes (RANS) equations is used to investigate the aerodynamic performance of the Flying-V aircraft configuration in the twin-aisle and single-aisle classes. Lift-constrained drag minimization is performed at the start-of-cruise operating point with the aircraft planform fixed and free. Aircraft weights are estimated using empirical methods. The planform-fixed case has design freedom in section shape and twist, while planform-free cases add chord, span, and sweep angles. At a cruise static margin of 6% and an altitude of 13,000 m, exclusive of nacelles, pylons, and excrescences, the optimized fixed-planform twin-aisle-size Flying-V aircraft produces a cruise lift-to-drag ratio of 25.5. Planform optimization, which reduces chord and sweep and increases span, enables a cruise lift-to-drag ratio of 26.7 at the same altitude. The optimized single-aisle-size Flying-V aircraft produces cruise lift-to-drag ratios of 20.2 and 23.2 at altitudes of 10,973 m and 13,711 m, respectively, again excluding drag contributions from nacelles, pylons, and excrescences. High-fidelity aerodynamic optimization shows that the Flying-V aircraft is capable of excellent aerodynamic performance at cruise. Strong shocks are absent on all optimized designs. The configuration excels in the twin-aisle class and attains sufficient aerodynamic performance at the single-aisle size to justify further study.

Nomenclature

A	=	Projected area of the aircraft [m^2]
C_D	=	Total drag coefficient of the aircraft
C_L	=	Total lift coefficient of the aircraft
C_m	=	Total pitching moment coefficient of the aircraft taken about the center of gravity
C_p	=	Pressure coefficient
CG1	=	Optimized twin-aisle-size planform-fixed Flying-V aircraft with CG at 83.1% MAC
CG2	=	Optimized twin-aisle-size planform-fixed Flying-V aircraft with CG at 87.1% MAC

*M.A.Sc. Candidate, rassam.yazdi@mail.utoronto.ca

†Research Associate, tom.reist@utoronto.ca

‡University of Toronto Distinguished Professor in Computational Aerodynamics and Sustainable Aviation, david.zingg@utoronto.ca

CG3	=	Optimized twin-aisle-size planform-fixed Flying-V aircraft with CG at 89.6% MAC
CG4	=	Optimized twin-aisle-size planform-fixed Flying-V aircraft with CG at 92.1% MAC
c	=	Chord at a given span station [m]
D	=	Total drag of the aircraft [N]
K_n	=	Static margin [% MAC]
L	=	Total lift of the aircraft [N]
L/D	=	Lift-to-drag ratio of the aircraft
MAC	=	Mean aerodynamic chord
MTOW	=	Maximum takeoff weight [kg]
MFW	=	Maximum fuel weight [kg]
N	=	Number of grid nodes
NP	=	Neutral point as measured from the aircraft nose, normalized by mean aerodynamic chord
OEW	=	Operating empty weight [kg]
SA Low Altitude	=	Optimized single-aisle-size Flying-V aircraft at a cruise altitude of 10.973 m
SA High Altitude	=	Optimized single-aisle-size Flying-V aircraft at a cruise altitude of 13.411 m
W	=	Aircraft weight at the start of cruise [N]
TA 1-Point	=	Single point-optimized twin-aisle-size planform-fixed Flying-V aircraft at Mach 0.85
TA 2-Point	=	Two point-optimized twin-aisle-size planform-fixed Flying-V aircraft at Mach 0.85 and 0.9
TA Planform Free	=	Optimized twin-aisle-size planform-free Flying-V aircraft
TA Planform Fixed	=	Optimized twin-aisle-size planform-fixed Flying-V aircraft
x/c	=	x-position as measured from the aircraft nose, normalized by local chord
y/b	=	y-position as measured from the aircraft centerline, normalized by span

I. Introduction

As a growing source of greenhouse gas emissions, the aviation industry faces increased pressure to reduce its environmental footprint. The International Civil Aviation Organization has asserted a goal of making the industry net-zero carbon-dioxide by 2050 [1], which demands immediate action on the part of aircraft manufacturers. While advances in the aerodynamics, structures, and propulsion disciplines have enabled significant improvements in fuel efficiency, the configuration of commercial aircraft remains unchanged. The conventional tube-and-wing (CTW) concept has prevailed for the past seven decades, implying that a step change in fuel efficiency may not be possible without the adoption of novel aircraft configurations [2–4]. In recent times, the truss-braced wing (TBW) and blended wing-body (BWB) configurations have garnered considerable attention. In January 2023, NASA awarded Boeing a contract to build

and test a full-sized transonic TBW demonstrator with an intent to reduce fuel burn by 30% [5]. Moreover, JetZero is preparing to fly a NASA-supported BWB demonstrator later this year, with the goal of having their aircraft delivered to customers by 2030 [6]. A configuration with a smaller share of the spotlight is the flying-wing concept, which aims to integrate lift, trimming, and payload carriage into a single component, removing the need for a fuselage [7].

Flying wings can still be viewed as a novel configuration despite their long-standing existence, as they have yet to be adopted for commercial use. Pioneering examples of the flying-wing concept can be traced back to the 1930s with Horten's Ho 229 fighter/bomber, and the 1940s with Northrop's YB-49 prototypes [8]. Stability and control, especially outside of the cruise mission phase, have historically posed great challenges in developing these aircraft. With the prevalence of augmented stability flight control systems, this particular area of concern is diminishing in severity [8]. The penalty associated with designing non-cylindrical cabins still remains an important area of further research. However, the aerodynamic and structural benefits associated with the flying-wing are notable. They are known for low drag by reducing wetted area with the removal of a dedicated fuselage component. Moreover, the configuration also allows for an improved weight distribution along the wingspan, which can lead to a lighter aerostructure [2]. Similar to BWBs, placement of engines above the planform's trailing edge effectively shields the ground from engine noise in low-altitude flight. A renowned example of a flying-wing aircraft is the Northrop B-2 bomber, which was designed as a pure flying-wing not only to reduce its radar cross section, but also to realize the substantial aerodynamic efficiency offered by this configuration [9].

A flying-wing concept that has gained popularity recently is the Flying-V, known for its distinct V-shaped planform [10]. Benad published the first paper on the Flying-V configuration in 2015 [11]. A preliminary performance analysis using a 3-dimensional vortex lattice method estimates that the Flying-V aircraft attains a 10% higher lift-to-drag ratio than the Airbus A350-900, with absolute figures omitted for confidentiality. At low speeds, the Flying-V is stated to be capable of matching the A350-900's reference speed of 150 kts at ISA + 15 with an angle of attack of less than 10 degrees. Next, Faggiano et al. [8] describe aerodynamic design work performed on the Flying-V configuration in the twin-aisle class. The aircraft is modelled with winglets but without engine nacelles and pylons, with contributions to profile drag from the latter determined empirically. A two-step optimization process is used, the first using a vortex lattice method to explore the design space and the following step making use of an inviscid flow solution based on the Euler equations paired with a skin-friction drag estimate. The optimized aircraft is reported to have a lift-to-drag ratio of 23.7, representing a 25% improvement over the NASA Common Research Model, which is adopted as a performance benchmark. The results also show the Flying-V aircraft to suffer from shock formation around the leading-edge of the inner wing and on the mid-chord portion of the outer wing. Since aerodynamic optimization using the Euler equations cannot account for shock-induced separation effects, the transonic feasibility of the concept remains an open question.

Moving to higher-fidelity aerodynamic analysis, van Luijk and Vos [12] performed planform-fixed aerodynamic shape optimization based on the RANS equations on the outer wing of the Flying-V, leaving the rest of the aircraft's

section shapes unchanged. The outer wing is granted freedom in section shape and twist using free-form deformation volumes. The optimization resulted a lift-to-drag ratio of 20.3, a step back from the previous figure. The inclusion of a straight control-surface hinge line and limited design freedom were seen to be responsible for the loss of performance. Additionally, strong shocks persist over the outer-wing. Laar et al. [13] built off the work done by van Luijk and removed the straight hinge line from the model and hand-selected section shapes to improve the performance of the aircraft. The best design attains a cruise lift-to-drag ratio of 24.2 at an angle of attack of 3.6 degrees with a cruise static margin of 2%, falling close to but still in excess of the deck angle constraint of 3 degrees. The presence of strong shocks is still reported around mid-span of the outer-wing and along the centerline, while drag is reported to ramp up dramatically at Mach numbers exceeding 0.85. Numerical optimization of the complete aircraft with high sectional and planform design freedom and an appropriate suite of constraints could lead to achieving improved performance without violating any design requirements such as deck angle.

Aerodynamic shape optimization based on the Reynolds-averaged Navier-Stokes (RANS) equations is the state-of-the-art method for aerodynamic design at transonic speeds. The work of Osusky and Zingg discusses the importance of using the RANS equations for better capturing the impact of viscous components of drag and local flow behaviours during aircraft design [14]. This approach has been extensively applied to unconventional aircraft configurations such as the BWB and TBW [15, 16]. The present paper, which expands on Yazdi et al. [17], applies high-fidelity aerodynamic optimization based on the RANS equations to the Flying-V aircraft configuration to provide an assessment of its fuel efficiency potential in the twin-aisle and single-aisle classes, representing the two largest market segments in the industry [18]. The twin-aisle-size Flying-V is sized to match the payload and range of the Airbus A350-900, while the single-aisle variant is matched to the Airbus A320neo. The objectives of this work are 1) to corroborate cruise performance results obtained by Faggiano et al. [8], 2) to demonstrate that wave drag can be sufficiently reduced, 3) to investigate the scalability of the concept by assessing a single-aisle class Flying-V aircraft, and 4) to study the performance improvements possible through increased planform freedom. Low-speed stability and control, field performance, mass properties analysis, multi-mission design, and powerplant sizing are left as areas of future work, potentially making use of the framework and formulation developed by Gray and Zingg [19].

II. Initial Geometry Preparation

A. Development of a Twin-Aisle-Size Flying-V Aircraft Baseline Geometry

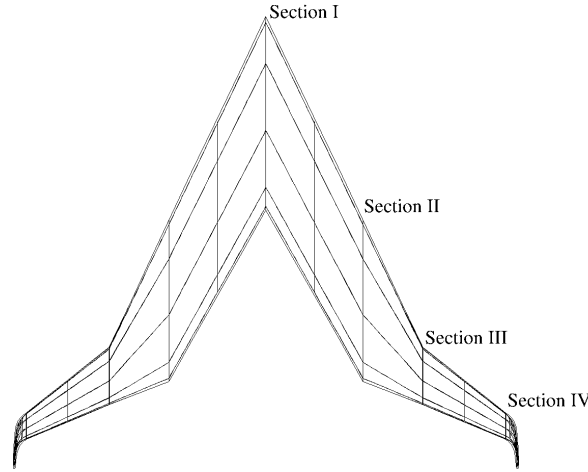
The baseline geometry for a twin-aisle-size Flying-V aircraft adopts the planform developed by Faggiano et al. [8], which is designed to match the top level requirements of the Airbus A350-900, a modern, state-of-the-art twin-aisle commercial aircraft. These include a payload of 440 passengers, a nominal range of 14,350 km, and a cruise Mach number of 0.85 at an altitude of 13,000 m [8]. The planform is obtained through design tables and diagrams available in

Table 1 General information regarding the baseline aircraft planform.

Planform Area [m ²]	Full Span [m]	Root Chord [m]	Tip Chord [m]
883.3	65.0	24.0	3.2

Table 2 Sectional breakdown of aircraft planform.

Sections	Leading Edge Sweep [°]	Quarter-Chord Sweep [°]	Taper Ratio [-]	Aspect Ratio [-]
I-II	64.40	63.50	0.833	1.12
II-III	64.40	59.21	0.354	1.17
III-IV	37.80	34.85	0.455	4.71

**Fig. 1 Defining the four major sections of the baseline aircraft planform definition.**

Faggiano et al. and TU Delft’s Flying-V website [10]. A full three-dimensional surface model is then created using the geometry toolbox developed by Gagnon and Zingg known as Genair [20]. A breakdown of the planform geometry is given in Tables 1 and 2, with definitions of aircraft sections provided in Fig. 1 and a 3D model is shown in Fig. 2.

The outboard wing is given a dihedral of 3 degrees, and the cabin-carrying portion of the aircraft is modelled without dihedral. The aircraft model also includes winglets. Nacelles and pylons are not modelled on the aircraft. The geometry used to initialize optimizations uses SC(2)-0014 sections [21] for the inboard portion of the aircraft, that is, up to the trailing-edge kink in the planform (section II), to maintain sufficient thickness to house the cabin. For the outboard wing, starting at the leading-edge kink (section III) up to the winglet (section IV), SC(2)-0012 sections are used. The winglet uses the SC(2)-0010 sections. For the initial geometry, airfoil shapes are linearly interpolated in the transition region between sections II and III.

A rectangular-cross-section passenger cabin is considered as opposed to the ovoidal shape chosen by Faggiano et al. to give the optimizer further shaping freedom on the leading edge despite enclosing the same amount of useful volume. The rectangular cabin is sized such that it is coincident with the oval defined by Faggiano et al. Eccentricities due to

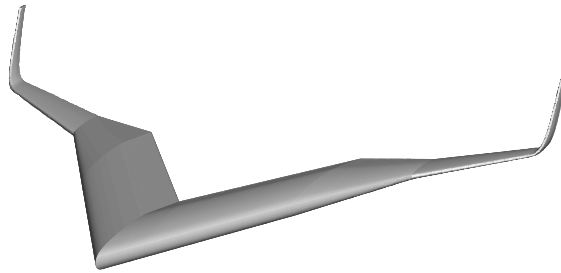


Fig. 2 Baseline Flying-V 3D model produced by the Genair geometry toolbox.

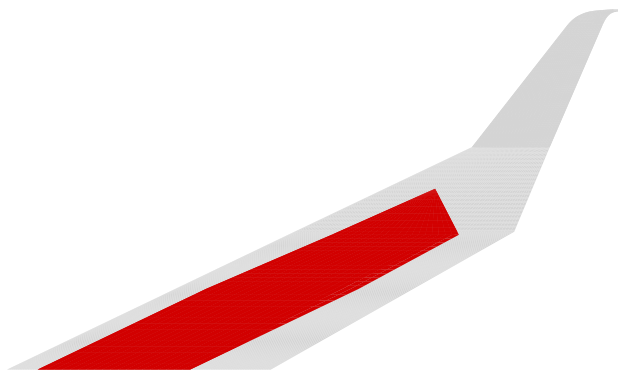


Fig. 3 Cabin shape within the baseline Flying-V aircraft planform.

cockpit and mid-line cabin transition are not modelled. However, this study does explicitly model the cargo cabin as an extension outboard of the passenger cabin, with a cross-sectional width, perpendicular to the leading edge, of 5 m and a minimum height of 1.63 m, equivalent to that of a unit load device (ULD) [22]. Calculation of the total cargo volume available in the model agrees well with the required volume of 172.4 m³ [8] and 14 ULDs per wing [10]. Figure 3 shows the cabin shape within the aircraft planform.

Throughout this study, the Flying-V aircraft are optimized at the start-of-cruise condition. Low-speed performance in the takeoff and landing segments of flight, stability and control, and detailed weight and balance considerations, which are important drivers in aircraft design, are left as avenues of future work. The scope of this study is largely aerodynamic, with the goal of finding an aerodynamic optimum rather than an aircraft-level optimum. An empirical weight estimation method has been developed to predict the weight of aircraft with varying planforms (segment chord, sweep, and span) and efficiencies (lift-to-drag ratio) to be able to impose a lift constraint at the start-of-cruise operating point. This method integrates two well-established approaches: Torenbeek's method for conventional aircraft components such as

Table 3 Validation of empirical weight estimation against reported Flying-V aircraft family weights [24].

	Flying V-800		Flying V-900		Flying V-1000	
	Oosterom and Vos	Estimate	Oosterom and Vos	Estimate	Oosterom and Vos	Estimate
OEW [10^3 kg]	90	90	112	110	127	124
Fuel [10^3 kg]	53	53	82	81	98	98
MTOW [10^3 kg]	171	171	225	222	259	256

wings, engines, and landing gear [2], and Bradley’s method for estimating the weight of the non-cylindrical pressure vessel and inner-wing structure. Torenbeek’s fuel fraction method [23] is used to calculate fuel weights for the aircraft. To validate the weight estimation method, the weight of three Flying V designs discussed by Oosterom and Vos [24], representing a family of aircraft based on the A350-800, -900, and -1000, are estimated and compared in Table 3. Maximum takeoff weights (MTOWs) agree to a precision of approximately 1% when compared to Oosterom and Vos [24]. The center-of-gravity (CG) positions for aircraft designs investigated in this study are chosen rather than calculated. They are positioned to be some percentage of mean aerodynamic chord (MAC) ahead of the neutral point by the end of optimization to satisfy static margin requirements, assuming that aircraft components, internally and externally, can be shifted to cater to the aerodynamically preferred CG.

B. Sizing of a Single-Aisle-Size Flying-V Aircraft

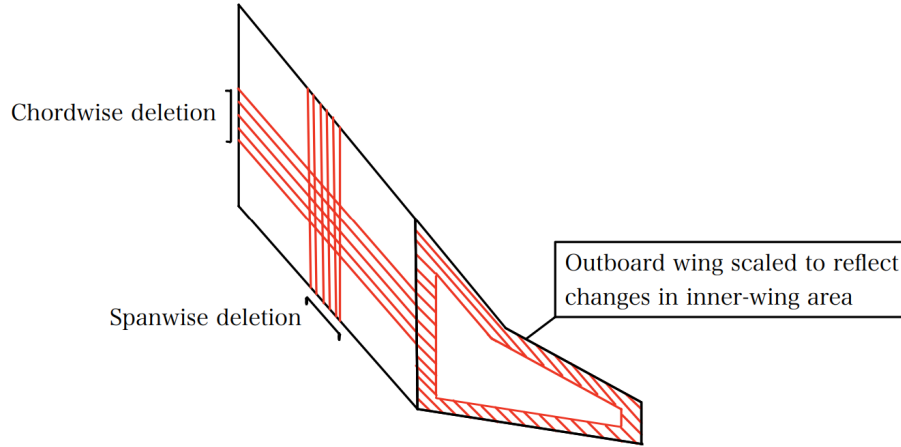
The Flying-V configuration is also modelled at the single-aisle size, which represents the largest market segment in the industry. Since there is no reference design for a Flying-V aircraft in this class, the twin-aisle-size aircraft is sized down to provide a baseline geometry. The baseline twin-aisle-size Flying-V aircraft is scaled down in three dimensions by reducing its MAC from 18 m to 10.8 m for the baseline single-aisle variant via the following formula:

$$L_{SA} = L_{TA} \left(\frac{A_{SA}}{A_{TA}} \right)^{0.5} \quad (1)$$

where L_{SA} , L_{TA} , A_{SA} , A_{TA} represent aircraft MAC and cabin floor area for the single-aisle and twin-aisle, respectively. The main assumption of Equation 1 is that the ratio of cabin floor areas of different aircraft classes approximately represents the scaling of their outer mold lines (OML). Table 4 summarizes the cabin design quantities based on the literature [25, 26], with volumes reported to further contextualize the size of the cabin. The scaling also brings the aircraft’s wing span close to compliance with Gate C constraints, which are imposed on single-aisle class aircraft. As this aircraft is sized to be significantly smaller than the twin-aisle, changes in the aerodynamically optimal planform and cabin layout are expected. Optimizations will include planform freedom to help determine the optimal cabin layout for a Flying-V aircraft of this size and to further help with satisfying the cabin shape constraint. The inclusion of other design disciplines would be required to identify the planform that attains the best all-around performance.

Table 4 Passenger and cargo cabin floor area and volume information.

	Single-Aisle		Twin-Aisle	
	Floor Area [m ²]	Volume [m ³]	Floor Area [m ²]	Volume [m ³]
Passenger	108.6	228.1	272.2	571.7
Cargo	32.8	37.4	120.3	172.4
Total	141.4	265.5	378.0	744.1

**Fig. 4 Chordwise and spanwise deletion scheme.**

C. Geometric Analysis of Flying-V Planform Variations

To examine how the wetted area benefit of the Flying-V aircraft changes with scale (single-aisle, twin-aisle, etc.) and proportions (longer span, shorter chord, etc.), a geometric investigation is undertaken. Since the baseline Flying-V design is at the twin-aisle size, the largest size investigated in this study, deletions are used. Two deletion fractions are used to scale the cabin-fitting portion of the aircraft:

- **Chordwise deletion fraction:** fraction of inboard chord
- **Spanwise deletion fraction:** fraction of inboard span

The outer wing area is scaled to match the reduction of area experienced on the inboard portion of the aircraft as a result of the deletions. Note that negative deletion fractions represent an addition. The scheme is shown in Fig. 4.

A grid of spanwise deletion fractions ranging from -1 to 1 and chordwise deletion fractions of -0.5 to 0.5 is generated, for which contours of floor area (A_{floor}), wetted area-to-floor area ratio (S_{wet}/A), wetted aspect ratio (AR_{wet}), and maximum thickness-to-chord ratio (t/c_{max}) are plotted in Fig. 5. There are two cabin floor area contours at 141.4 m² and 378 m², which represent the floor area required by a single-aisle and twin-aisle-size aircraft, respectively. Wetted aspect ratio grows as the chord shrinks and span increases, while the wetted area-to-floor area ratio shrinks moving toward the top right of the plot. This suggests that planform-optimized designs should move toward the right on their

elasticity model is used to propagate B-spline control point deformations in parallel across the B-spline volume. The grid parametrization scheme is also capable of generating additional grid levels, automatically inserting and redistributing grid nodes, which maintains baseline grid spacing functions [28].

Geometry control is performed through a free-form and axial deformation method, where free-form deformation (FFD) volumes [29] provide local shape control, and global shape control is performed via axial curves that drive the FFD volumes [30]. FFD volumes are B-spline lattices that transform embedded objects as the volume deforms. Following Gagnon and Zingg, the B-spline control points that define the aerodynamic surface are embedded within the FFD volumes, ensuring that the analytical definition of the surface is maintained. Figure 6 displays the FFD volume and axial curves that parametrize the geometry of the Flying-V aircraft. The black grid represents the FFD volume enclosing the aircraft, and the green spheres represent axial control points, which are joined by green line segments

The optimization algorithm used in this study is a gradient-based method known as the Sparse Nonlinear OPTimizer (SNOPT) [31]. This type of optimizer is beneficial for this application given that it typically requires fewer function evaluations to converge on a solution when compared to gradient-free methods, such as genetic algorithms [32]. The consequence of this choice is the risk of finding only a local optimum on multimodal optimization problems, which can be addressed using the global optimization techniques discussed by Chernukhin and Zingg [33]. This approach is not used in this study, so reported optima may be local optima as opposed to a global optimum.

Finally, the evaluation of objective and constraint gradients used by SNOPT is performed using the discrete adjoint method, which is advantageous for problems with many more design variables than flow-dependent constraints. An efficient method for solving the resultant linear system is a modified, flexible version of the Generalized Conjugate Residual with Orthogonalization and Truncation (GCROT) algorithm [34], as the system must be solved deeply in order to obtain sufficiently accurate gradients. Details of the adjoint method and its integration are described by Hicken and Zingg [27].

The described framework has been extensively used for aerodynamic shape optimization in a variety of cases, inclusive of unconventional aircraft with significant planform freedom. Reist and Zingg performed high-fidelity aerodynamic shape optimization of a lifting-fuselage regional aircraft in 2017 [35], and later following it up with a multifidelity technique, which also included stability and control requirements in the problem formulation [15]. In 2020, the optimization framework was validated on a wing-body case against Bombardier Aerospace's in-house optimization algorithm, showing good agreement for both single and multi-point optimizations [36]. More recently, the framework has been used to investigate cruise drag reduction through the use of variable camber [37] and applied to the aerodynamic optimization of a single-aisle-class transonic strut-braced-wing aircraft [16].

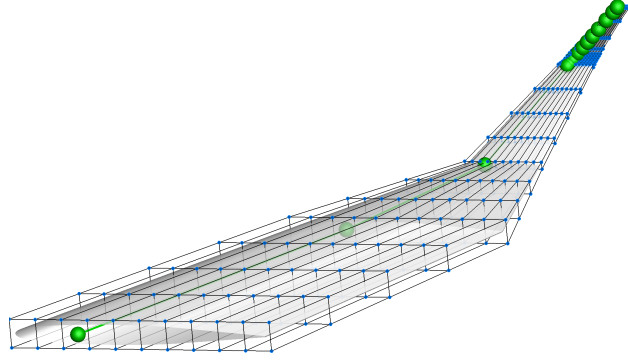


Fig. 6 Baseline Flying-V aircraft FFD volume (black) and axial control points (green).

IV. Optimization Problem Formulation

A. Overview of Optimization Cases

To provide a consolidated overview of the optimization cases discussed in this section, Fig. 7 presents a hierarchical diagram outlining the individual cases explored and the corresponding studies that motivated their inclusion. This figure serves to contextualize the optimization studies at a high level before going into the detailed discussion that follows.

B. Twin-Aisle-Size Flying-V Aircraft

RANS-based aerodynamic shape optimization is performed on the twin-aisle-size Flying-V aircraft at the start-of-cruise operating condition. The optimization objective is prescribed to be drag minimization subject to various aerodynamic and geometric constraints. Two driving aerodynamic constraints are the lift equality constraint and a trim constraint that dictates the pitching moment about the CG to be zero. Lift constraints are implemented by applying the empirical weight estimation method introduced in II.A to the initial geometry of a given optimization case, which is updated in successive optimization processes to reflect the weight of the optimized aircraft. Sequential optimizations are performed until the optimized aircraft's maximum takeoff weight (MTOW) differs by less than 1% when compared to the aircraft that initialized the resubmission. While seeking the aerodynamic optimum, weight analysis is kept accurate with respect to the weight estimation model. Geometric constraints include a minimum maximum thickness-to-chord ratio constraint of 11% between sections III and IV to reduce the likelihood of producing a structurally infeasible outboard wing in accordance with the thickness requirement set by van Luijk and Vos [12] and a cabin shape constraint that requires the cabin floor and ceiling to be enclosed by the aircraft OML. With symmetric airfoils and untwisted wing sections, the starting aircraft will not satisfy the lift and geometric constraints. The twin-aisle optimizations are divided into planform-fixed and planform-free problem formulations. While planform freedom allows for further exploration of the aircraft's aerodynamic optimum, the baseline planform is the product of considerations beyond aerodynamic efficiency [8], motivating planform-fixed optimizations.

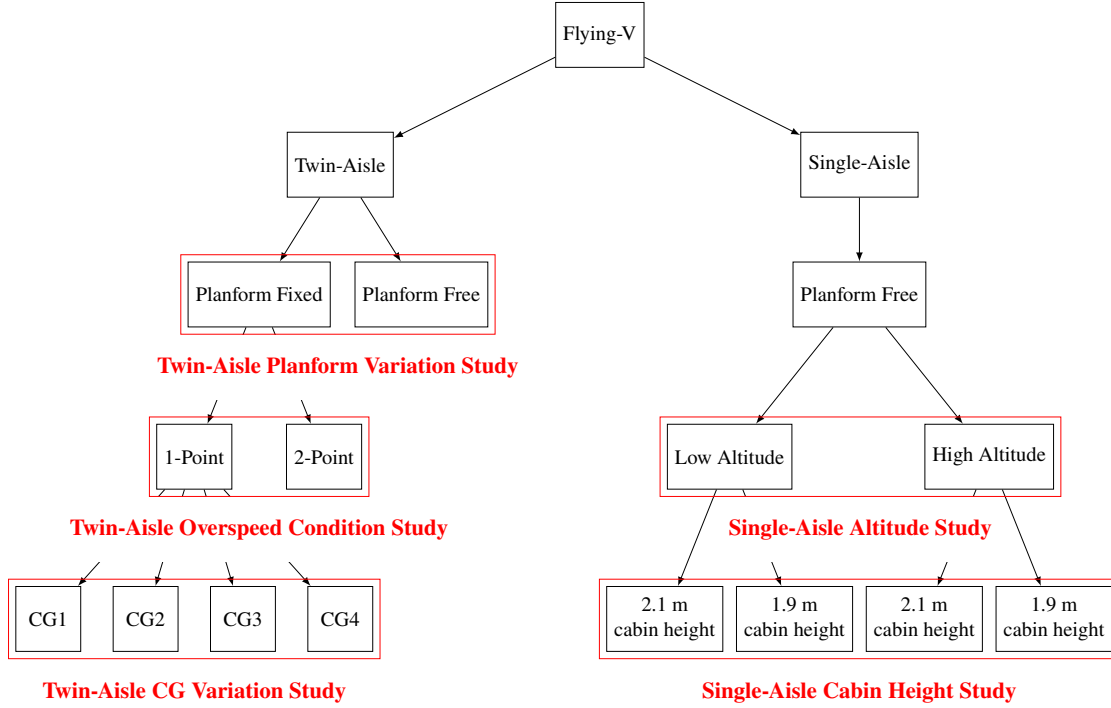


Fig. 7 Overview of Optimization Cases Studied

1. Planform-Fixed Optimization Formulation

Even with the planform fixed, there are many design variables for the optimizer to work with in order to minimize drag. The angle-of-attack is a design variable with bounds of ± 3 degrees, dictated by deck-angle requirements. The wing is divided into 4 segments, the most inboard segment with a near-unity taper, the mid-span transition region, the outboard wing that is noticeably less swept than the two inboard segments, and the winglet. Airfoil shapes are controlled at 5, 4, 5, and 11 span stations on each of the aforementioned segments, respectively. There are 22 FFD control points at each span station, split evenly between the lower and upper surfaces. The twist angle, which represents the rotation of the FFD volume cross-section about the axial curve, is free at all span stations, except at the aircraft centerline. The section shape variables can vary independently within the FFD volume. Table 5 presents the variables and constraints of the optimization. There are a total of 506 geometric design variables active during the optimization.

Additionally, using this problem formulation, an investigation is carried out to evaluate the performance sensitivity of the aircraft to CG positioning and hence static margin at cruise. Four CG positions, expressed as a percentage of MAC, are chosen to be investigated in this study in the vicinity of the baseline aircraft's neutral point: 83.1%, 87.1%, 89.6%, and 92.1% MAC, denoted CG1, CG2, CG3, and CG4, respectively. The initial aircraft's neutral point is located at 87.1% MAC. This study is discussed in Section V. An additional aircraft will be optimized with a CG positioned such that the *resulting optimized aircraft* has a static margin of 6% MAC. This aircraft is referred to as TA Planform Fixed.

Table 5 Design variables and constraints for planform-fixed twin-aisle optimizations. Numbers in parentheses give the number of each variable or constraint.

Variables		Constraints	
$-3^\circ \leq$	AoA (1)	$\leq 3^\circ$	$0.11 \leq$ Maximum thickness-to-chord ratio (5)
$-15^\circ \leq$	Twist (24)	$\leq 15^\circ$	Cabin shape surface
$5\% \leq$	Shape (481)	$\leq 200\%$	$L = W$
			$C_{M@CG} = 0$

2. Planform-Free Optimization Formulation

Planform-free optimizations are performed in two steps. First, to determine the aerodynamically optimal planform, a lift-to-drag ratio maximization is performed with no constraints on lift or pitching moment. Cabin airfoil maximum thickness and planform projected area constraints ensure that the cabin height is retained and floor area remains unchanged in the exploration of the optimal cabin layout. The optimization problem is summarized in Table 6, with chord length (three inner-most span stations) and axial control point position freedom, allowing for changes in sectional span and sweep angles which can be expressed as freedom in full aircraft span and inner-wing sweep. Bounds for planform design variables are specified to facilitate exploration in the design space close to the starting geometry to understand aerodynamic performance sensitivity rather than determining an optimum. The inner-wing taper ratio constraint retains the Flying-V shape.

Step one produces a planform with a reduced chord, reduced sweep, and a larger span, agreeing with the direction suggested by the geometric analysis. The change in geometry is contrasted with the baseline planform in Fig. 8. The cabin layout that fits best into the new planform is the 3-2-3 passenger/aisle layout, representing a reduction in width from 3-4-3. A rectangular cabin is modelled to enclose the required volume and surface area as specified in Table 4 with a cabin width that corresponds to the chosen layout. The cabin height is stepped down to the height of a ULD (1.63 m for twin-aisle-size aircraft) for the outboard portion that is to carry cargo pallets. The cabin floor area is kept constant between TA Planform Fixed and TA Planform Free. In line with TA Planform Fixed, a CG is chosen such that it produces a cruise static margin of 6% for the optimized aircraft at the end of step two. Once the exploratory first step is concluded, the resultant aircraft then becomes the starting point for step two. The second step follows the formulation shown for the planform-fixed case, fitting the new cabin within the new OML and re-implementing the full range of constraints including lift and trim. The problem formulation as shown in Table 5 is then repeated, re-implementing the weight estimation method as well. Between the two planforms shown, the structural weight of the baseline planform is 2000 kg lighter than that of TA Planform Free. While the reduction in weight from lowered inner-wing angle is negated by an increase in span and planform area to fit the new cabin layout, the planform changes do improve cruise lift-to-drag ratio by 7%.

Table 6 Design variables and constraints for step one of planform-free twin-aisle optimizations. Numbers in parentheses are the quantity of each variable or constraint.

Design Variables			Constraints	
$-3^\circ \leq$	AoA (1)	$\leq 3^\circ$	$0.11 \leq$	Maximum t/c - outboard wing (2)
$-15^\circ \leq$	Twist (24)	$\leq 15^\circ$	$3.3 \text{ m} \leq$	Cabin airfoil thickness (5)
$5\% \leq$	Shape (481)	$\leq 200\%$		Fixed sectional area (4)
$50\% \leq$	Chord (3)	$\leq 200\%$	$0.833 \leq$	Inner-wing taper ratio (1)
$55 \text{ m} \leq$	Span	$\leq 75 \text{ m}$		
$50^\circ \leq$	Inner-wing sweep	$\leq 80^\circ$		

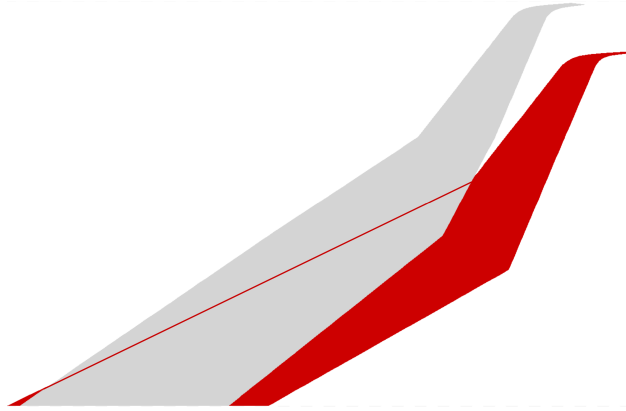


Fig. 8 Comparison of the exploratory optimized planform (grey) with the baseline planform (red).

3. Two-Point Optimization: Overspeed Considerations

A two-point optimization is carried out on the twin-aisle-size Flying-V aircraft to improve performance at cruise speeds higher than the nominal Mach 0.85 and assess the resultant penalty incurred at the nominal speed. At each operating condition, the formulation mirrors the TA Planform Fixed optimization case in geometric freedom and objective (drag minimization), with details shown in Table 7. The trim condition is enforced at $M = 0.85$. Within the multipoint objective function definition, the nominal $M = 0.85$ cruise condition is assigned twice the weight of the overspeed condition at $M = 0.90$. The design obtained from this optimization will be referred to as TA 2-Point, while for results comparison and discussion, TA Planform Fixed will be referred to as TA 1-Point.

C. Single-Aisle-Size Flying-V Aircraft

For the single-aisle-size Flying-V aircraft, the initial geometry for the optimizations is the scaled-down baseline twin-aisle-size planform discussed in Section II.B. The two-step process outlined in Section IV.B.2 for the planform-free optimization of the twin-aisle-size Flying V aircraft is roughly repeated at the single-aisle-size. Lift-to-drag ratio maximization is performed at a Mach number of 0.78, which is the nominal cruise speed for single-aisle aircraft [23], to obtain the starting geometry for the second step. Design variables and constraints for the second step align with what was previously shown in Table 6. A 3-3 cabin layout is seen to best suit the resultant planform. Step two in this study is

Table 7 Design variables and constraints for planform-fixed twin-aisle-size optimizations. Numbers in parentheses give the number of each variable or constraint.

Variables			Constraints	
Point 1: M 0.85				
$-3^\circ \leq$	AoA (1)	$\leq 3^\circ$	$0.11 \leq$	Maximum thickness-to-chord ratio (5)
$-15^\circ \leq$	Twist (24)	$\leq 15^\circ$		Cabin shape surface
$5\% \leq$	Shape (481)	$\leq 200\%$		$L = W$
				$C_{M@CG} = 0$
Point 2: M 0.90				
$-3^\circ \leq$	AoA (1)	$\leq 3^\circ$	$0.11 \leq$	Maximum thickness-to-chord ratio (5)
$-15^\circ \leq$	Twist (24)	$\leq 15^\circ$		Cabin shape surface
$5\% \leq$	Shape (481)	$\leq 200\%$		$L = W$

Table 8 Design variables and constraints for step two of single-aisle optimizations. Numbers in parentheses are the quantity of each variable or constraint.

Variables			Constraints	
$-3^\circ \leq$	AoA (1)	$\leq 3^\circ$	$0.11 \leq$	Maximum thickness-to-chord ratio (2)
$-15^\circ \leq$	Twist (24)	$\leq 15^\circ$		Cabin shape surfaces (2)
$5\% \leq$	Shape (481)	$\leq 200\%$		$L = W$ (1)
$50\% \leq$	Chord (3)	$\leq 200\%$		$C_{M@CG} = 0$ (1)
$28 \text{ m} \leq$	Span	$\leq 48 \text{ m}$		
$50^\circ \leq$	Inner-wing sweep	$\leq 80^\circ$		

performed differently than it is for the twin-aisle planform-free optimizations - the planform is free to better facilitate the cabin fitting process. This relaxation was not required for step two of the twin-aisle planform-free optimizations. Table 8 describes the specific design variables and constraints in the optimization formulation. Additionally, the cargo section of the cabin is modelled with a ULD height of 1.14 m, which is the norm for single-aisle pallets [26], allowing for thinner outboard cabin airfoils.

The lift constraint is implemented using the method discussed in Section IV.B. The single-aisle-size aircraft is investigated at two altitudes. The Flying-V aircraft tends to be more efficient at higher cruise altitudes; however, single-aisle aircraft missions often involve a relatively short cruise segment, so this benefit can be outweighed by the increase in fuel needed to climb to the higher altitude. The altitudes selected for each optimization are 10,973 m and 13,411 m, which correspond to 36,000 ft and 44,000 ft, respectively. The low- and high-altitude single-aisle-size Flying-V designs will be referred to as SA Low Altitude and SA High Altitude, respectively. Both single-aisle-size aircraft have CGs positioned such that the optimized aircraft have a cruise static margin of roughly 6%.

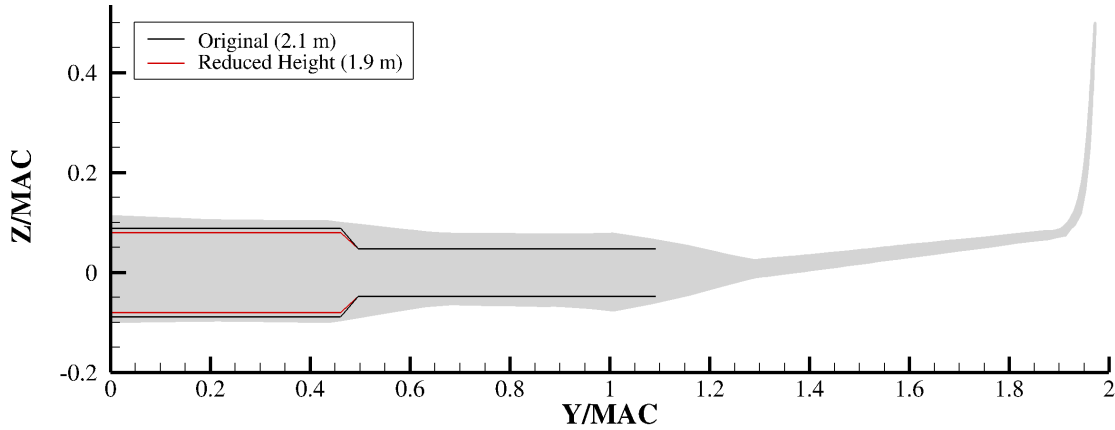


Fig. 9 Passengers and cargo cabin surfaces within original height optimized geometry (black and red lines). Outboard cargo-housing portion remains unchanged.

1. Cabin Height Study

Contouring of the aircraft OML against the leading and trailing edge portions of the cabin highlights its substantial design influence, prompting a quantification of its aerodynamic impact on the aircraft performance. A cabin-height study is performed by re-running the aforementioned single-aisle-size optimization cases with a reduced-height passenger cabin. The cabin constraint is modified on the inboard, cabin-housing portion, to have a height of **1.9 m** as opposed to the original **2.1 m**. Figure 9 illustrates the extent of the change, set within the starting geometry of both optimization cases (OML violations of cabin visible).

D. Grid Convergence

The Flying-V aircraft are optimized using grids of 1.7×10^6 nodes. Final force and moment coefficients are determined by performing a grid convergence study on the optimized design. For each design, three additional grids with two, four, and eight times the number of nodes in the grid used for optimization are created and used for flow evaluation. Richardson extrapolation is performed to estimate grid-converged performance. All performance results presented are Richardson extrapolated estimates. Figure 10 shows the convergence study performed on TA Planform Fixed, with the connected black-outlined markers representing flow evaluation results and the red marker representing the Richardson extrapolated drag coefficient. This study is performed at constant C_L . The four principal optimization cases (TA Planform Free, TA Planform Fixed, SA Low Altitude, SA High Altitude) were also repeated on a finer grid with 3.4×10^6 nodes to study the impact of grid density on the optimal designs. Results discussed in Section VIII show its impact to be small.

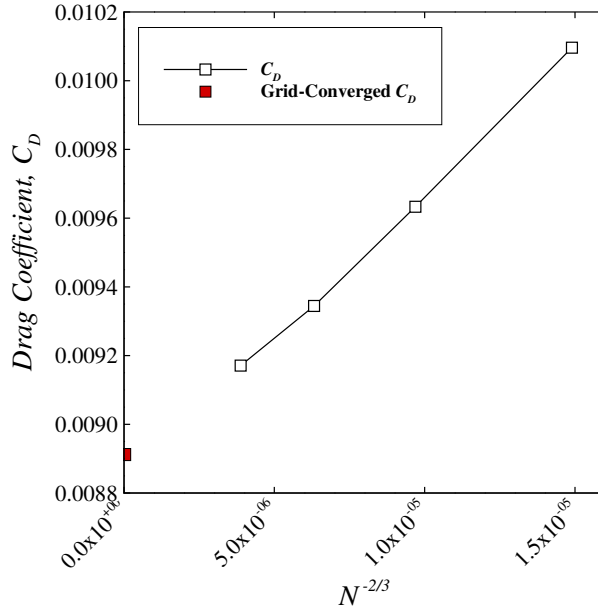


Fig. 10 Baseline twin-aisle-size Flying-V aircraft grid convergence study at Mach 0.85 and $C_L = 0.262$. N represents the number of grid nodes.

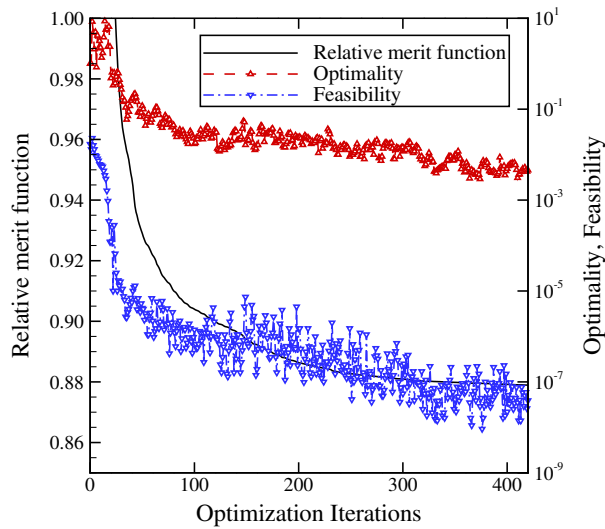


Fig. 11 Optimization history for the TA Planform Fixed Flying-V aircraft optimization case.

E. Optimization Convergence

Optimization convergence is measured with three metrics. The primary metric is the merit function, which is effectively the objective function once the constraints are satisfied. Next, optimality represents the gradient of an augmented objective, and finally, feasibility quantifies the degree to which the constraints are satisfied. All optimizations presented are continued until the merit function attains a plateau, while the optimality and feasibility drop at least three and six orders, respectively. Figure 11 shows the optimization history associated with the TA Planform Fixed design.

Table 9 Performance of optimized twin-aisle-size aircraft at the start of cruise.

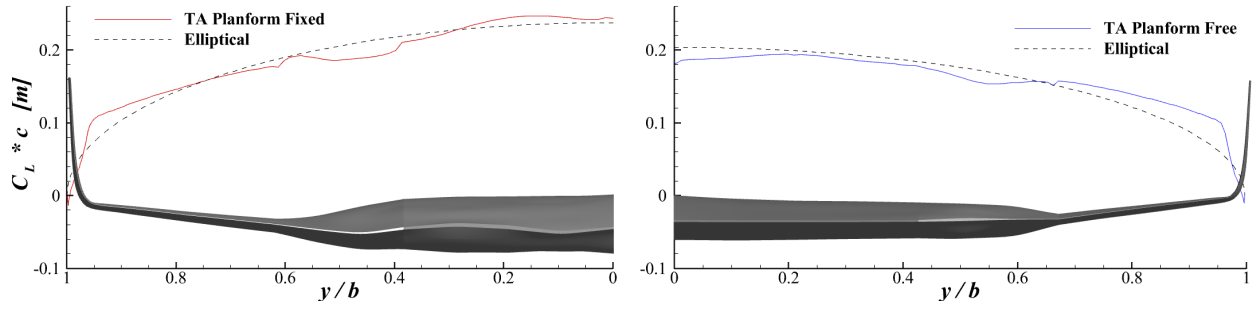
Parameter	TA Planform Fixed	TA Planform Free	A350-900
MTOW [kg]	220,600	218,500	283,000
Planform Area [m ²]	883	970	443
Span [m]	65.0	75.0	65.0
Inner-Wing Sweep [deg]	65	55	
AR _{wet} [-]	2.59	3.31	
Altitude [m]	13,000	13,000	
C_L [-]	0.262	0.234	
C_D [-]	0.0103	0.0088	
L/D [-]	25.5	26.7	

V. Twin-Aisle-Size Flying-V Aircraft Results and Discussion

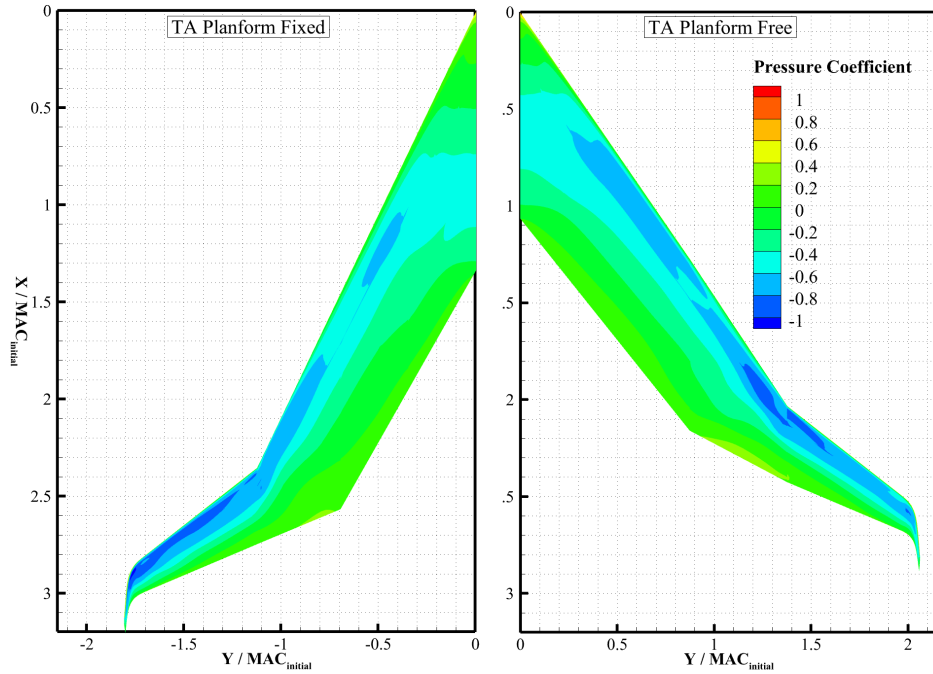
This section will discuss the results obtained from optimization performed on the twin-aisle-size Flying-V aircraft. Table 9 breaks down the performance of the two twin-aisle-size aircraft with a 6% static margin. TA Planform Free has a 5% greater lift-to-drag ratio and a lower weight due to a lighter fuel load and lower sweep angle. Compared to the predicted maximum takeoff weight of 225 000 kg quoted by Faggiano et al. [8], the weight estimation predictions for TA Planform Fixed and TA Planform Free are 2-3% lower, which is primarily derived from the lower fuel weight *. Compared to the A350-900 weight savings are substantial due to the assumed structural efficiency of the configuration within the weight model. As weight reduction is a significant driver of this concept’s fuel efficiency, further validation of the weight estimate would be beneficial. The optimization performed here is strictly based on aerodynamics, i.e. minimizing drag, and a multidisciplinary optimization is recommended for future work. The effect of the changes in span and sweep are accounted for in the weight model. The added weight due to the span increase for the planform-free case is offset by the reduced sweep and fuel weight.

The aerodynamic performance of the planform-fixed design, TA Planform Fixed, and the planform-free design, TA Planform Free, is shown in Fig. 12. Starting with TA Planform Fixed, the lift distribution of the aircraft roughly follows an elliptical shape. Sectional pressure distributions are shown at 6 span stations: the centerline (section I), start of transition region (section II), end of transition region (section III), and three positions along the outboard wing. The geometry is seen to be shock free with the exception of some weak shocks in the wing-winglet junction. Airfoils at the centerline and outer-wing stations are aft-loaded. There is a noticeable reduction in leading-edge radius starting at 45% span, which is expected as the cabin no longer drives shaping at that point. This aircraft accounts for the shape of the cargo hold outboard of the passenger cabin, so it is expected for the optimizer to encounter difficulties reducing section thickness in the transition region without violating the shape constraint. When comparing to Faggiano et al., their outboard wing sections feature a noticeable hook near the trailing edge [8], likely from using the Euler equations when optimizing. For TA Planform Free, the geometry of the aircraft is consistent with the wetted aspect ratio analysis

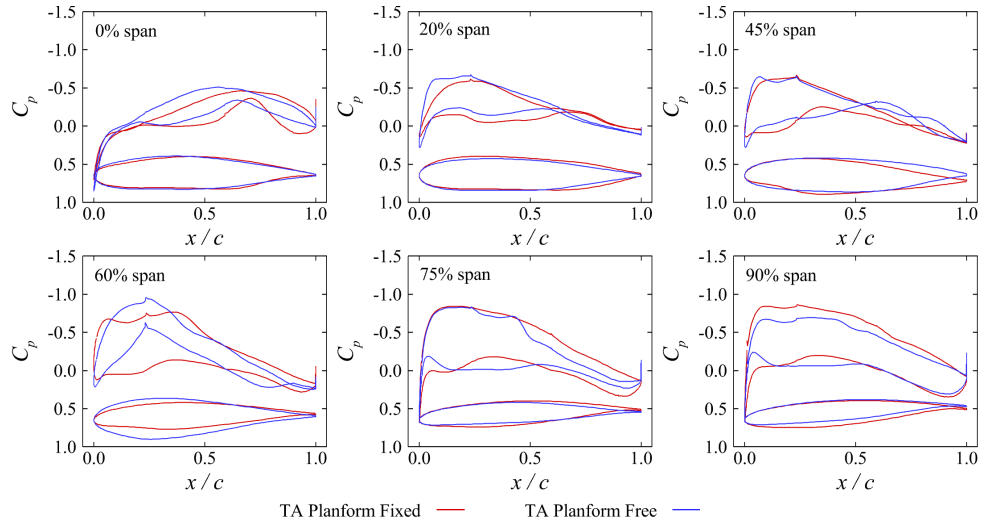
*The optimized design of Faggiano et al. attains a lift-to-drag ratio of 23.7 [8]



(a) Spanwise lift distribution



(b) Surface pressure distribution



(c) Sectional pressure distributions

Fig. 12 Solution information for twin-aisle-size Flying-V aircraft.

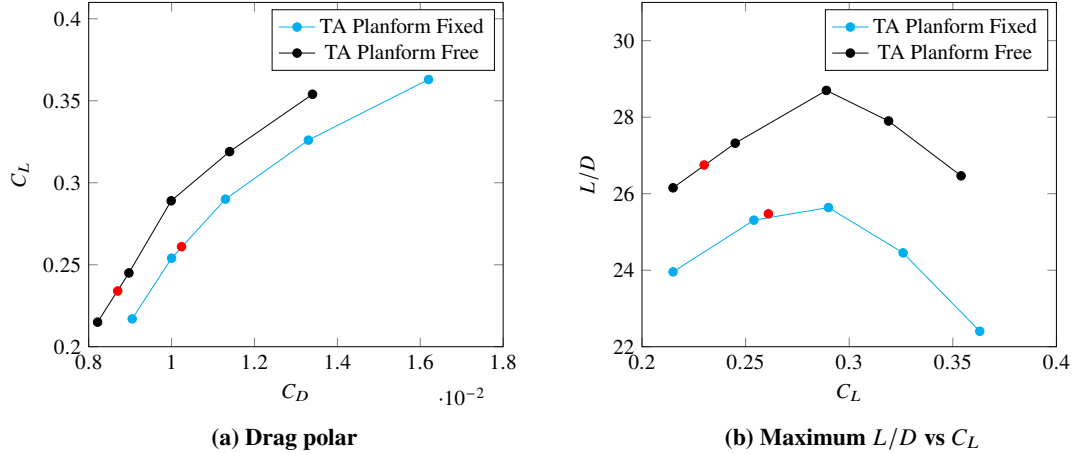


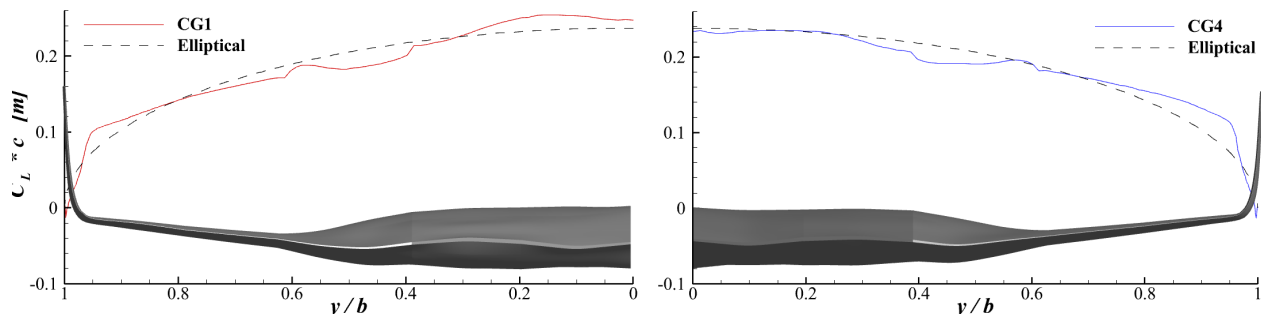
Fig. 13 Aerodynamic properties of the twin-aisle-size Flying-V aircraft (Mach 0.85, Reynolds number of 85 million). Red symbols represent optimization operating points.

Table 10 Performance sensitivity of optimized aircraft at the start of cruise.

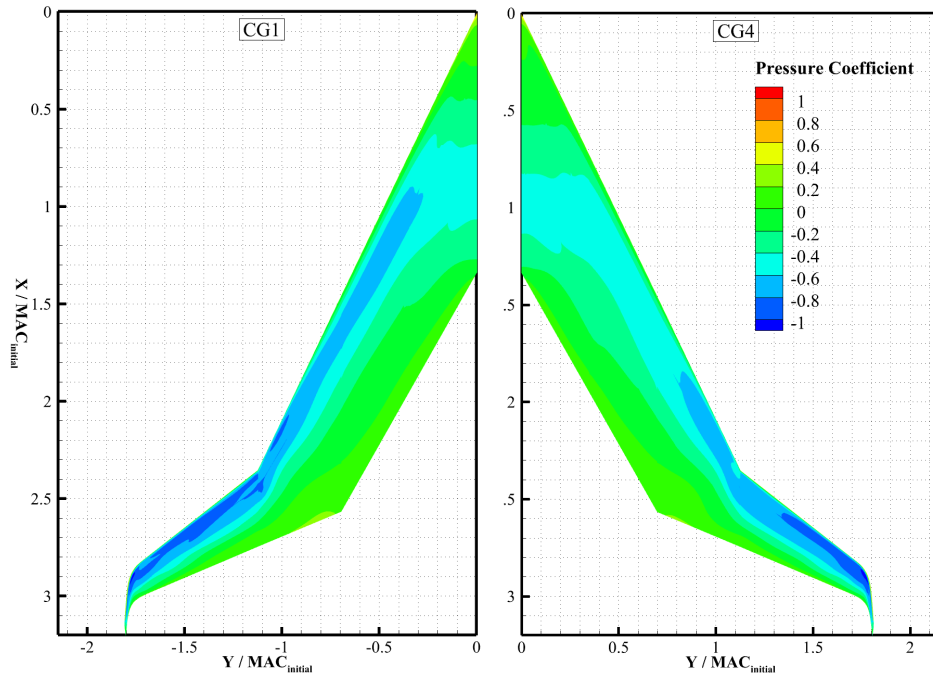
Design	AoA [deg]	C_L [-]	C_D [-]	L/D [-]	Resulting K_n [% MAC]
CG1	3.00	0.262	0.0105	25.0	8.8
TA Planform Fixed	3.00	0.262	0.0103	25.7	6.0
CG2	3.00	0.262	0.0102	25.7	5.1
CG3	3.00	0.262	0.0101	25.9	3.5
CG4	3.00	0.262	0.0100	26.0	1.7

performed in Section II.C, exhibiting a reduced chord and an increased span on the cabin-housing portion of the wing. The span constraint is active, with the optimized aircraft's span reaching the 75 m upper bound. Compared to the baseline, the inner-wing sweep of the optimized Flying-V aircraft is 10 degrees lower. Section shapes are consistent with TA Planform Fixed, except at 60% span, which is much thicker due to the reduction in inner-wing chord. No strong shocks are seen across the aircraft and pressure peaks are lower across the aircraft, consistent with the lower cruise C_L . Figure 13 displays the aerodynamic properties of the two aircraft, both of which would benefit from a higher cruise altitude, as their cruise lift coefficient would be closer to the lift coefficient that maximizes their lift-to-drag ratios. This is more pronounced for the TA Planform Free aircraft, as its cruise C_L is the lower of the two.

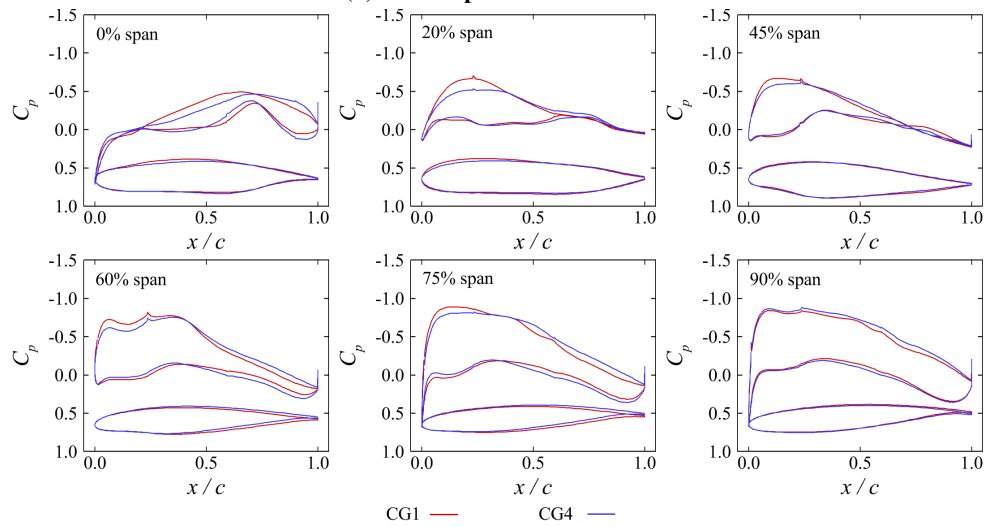
Results of the fixed-planform CG variation study are presented in Table 10 for the CG1, CG2, CG3, and CG4 aircraft, representing a static margin range of 7%. The CG4 aircraft, with the smallest static margin at 1.7%, has a 4.4% higher lift-to-drag ratio compared to CG1, which has a margin of 8.8%. The Flying-V concept exhibits heightened aerodynamic performance sensitivity to cruise static margin at values above 5%. A 2% lift-to-drag ratio benefit can be realized when reducing the cruise static margin from 6% to near-neutral stability. Figure 14 compares the aerodynamics of CG1 and CG4, as minimal solution change is seen moving from the forward-most to the aft-most CG position aircraft. Based on the lift and surface pressure distributions, it can be seen that CG1 produces more lift with the inner-wing and



(a) Spanwise lift distribution



(b) Surface pressure distribution



(c) Sectional pressure distributions

Fig. 14 Solution information for twin-aisle-size Flying-V aircraft with CG variations.

Table 11 Cruise performance of TA 1-Point and TA 2-Point twin-aisle-size planform-fixed aircraft.

Design	Mach [-]	C_L [-]	C_D [-]	L/D [-]
TA 1-Point	0.85	0.262	0.0103	25.5
	0.90	0.234	0.0102	22.8
TA 2-Point	0.85	0.262	0.0103	25.4
	0.90	0.234	0.0095	24.6

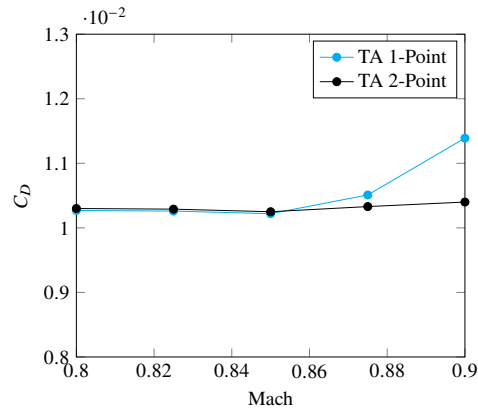


Fig. 15 Single and two-point optimized twin-aisle-size planform-fixed drag divergence at a constant C_L of 0.262.

less lift with the outer-wing relative to CG4, which has the aftmost CG. The sectional pressure distributions shows greater inner-wing loading for CG1 as well. The CG4 aircraft has flatter inner-wing airfoils, but differences in section shapes are generally small. Weak shocks seen on the inside of CG1's winglet are eliminated on the CG4 aircraft.

Two-Point Optimization: Aerodynamic Performance at Overspeed Condition

Drag rises substantially for the twin-aisle-size Flying-V aircraft as the cruise Mach number increases past Mach 0.85. To examine the performance penalty at the nominal cruise speed of Mach 0.85 for increasing the aircraft's drag divergence number, a second operating point is added to the optimization problem formulation. The results of the 2-point optimization point to a substantially improved performance at higher Mach numbers for a minimal penalty to performance at the nominal speed. Table 11 quantifies the change in performance between TA 1-Point and TA 2-Point Flying-V aircraft. For a 0.4% increase in drag at the nominal cruise Mach number of 0.85, a drag reduction of 7.8% is realized at the Mach 0.90 overspeed condition. Figure 15 illustrates the drag divergence properties of the two aircraft across a range of Mach numbers. The performance of TA 2-Point is balanced across the range of speeds examined, experiencing negligible drag rise as cruise Mach number increases to 0.90, with a very small performance cost below a Mach number 0.85. Sectional pressure distributions at Mach 0.90 are shown in Fig. 16. The TA 1-Point aircraft shows shock formation over the majority of the outer wing and portions of the cabin-housing wing, while the sectional pressure distributions of TA 2-Point show the elimination of strong shocks at a Mach number of 0.90, and hence the drag-divergence Mach number has been substantially increased with a very small performance penalty at Mach 0.85.

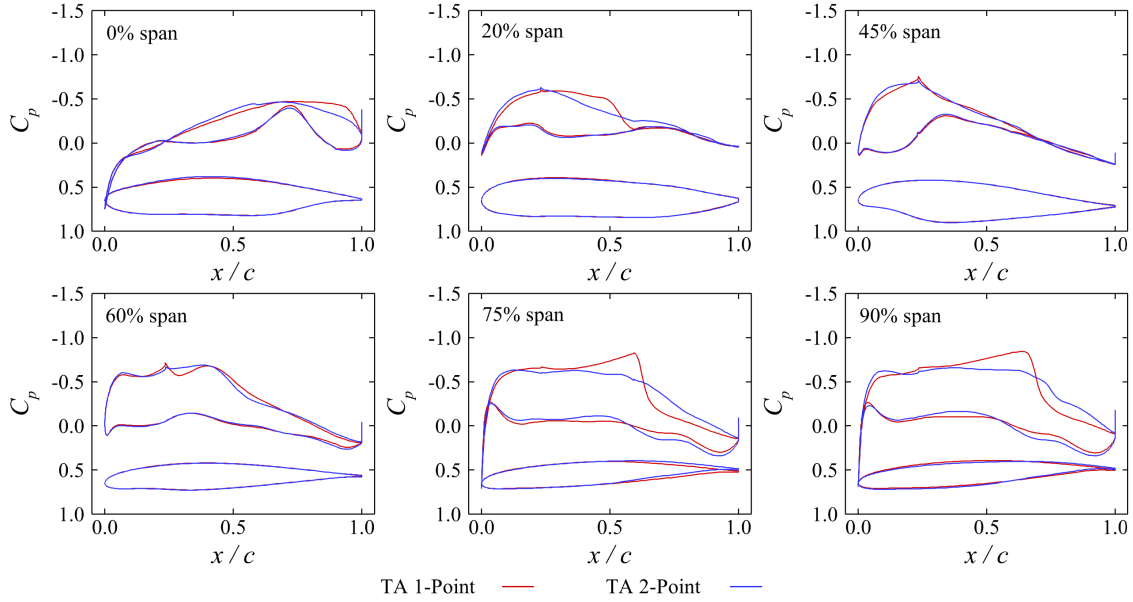
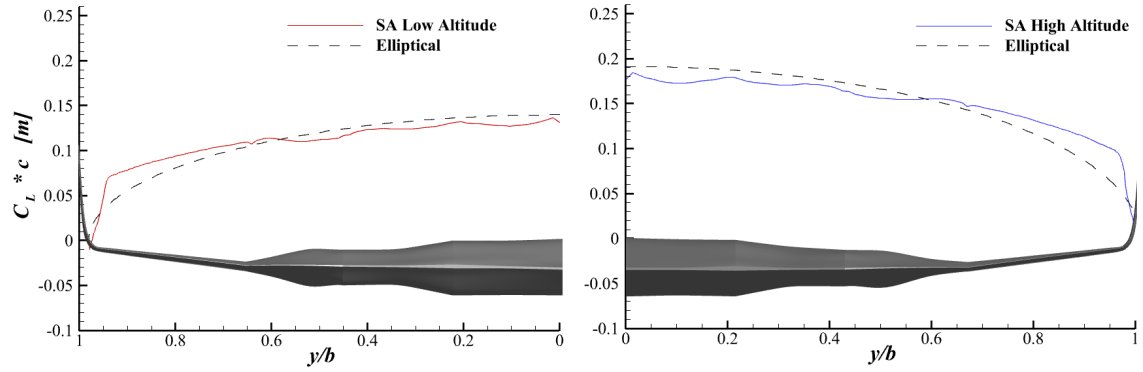


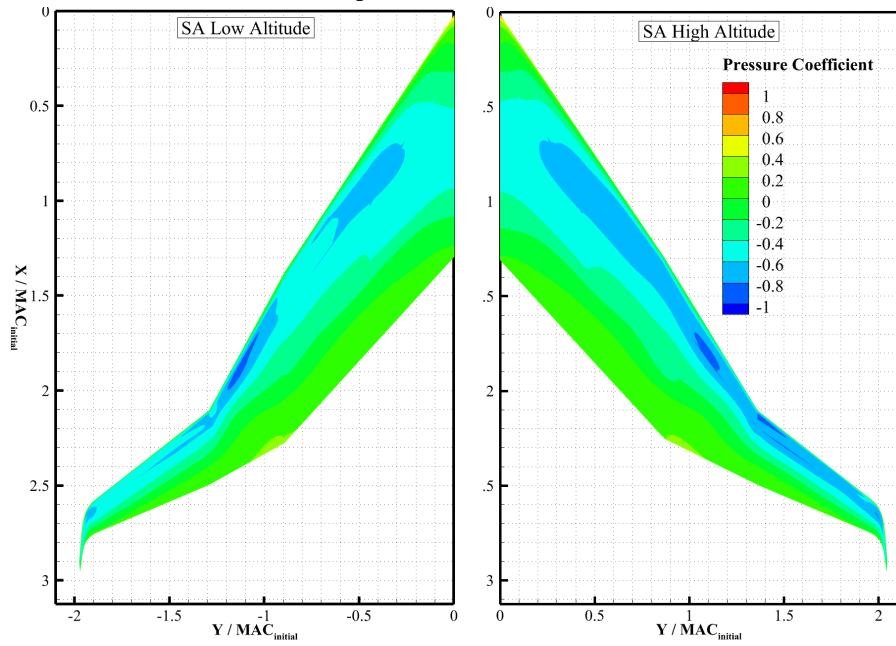
Fig. 16 Sectional pressure distributions at $M = 0.90$.

VI. Single-Aisle-Size Flying-V Aircraft Results and Discussion

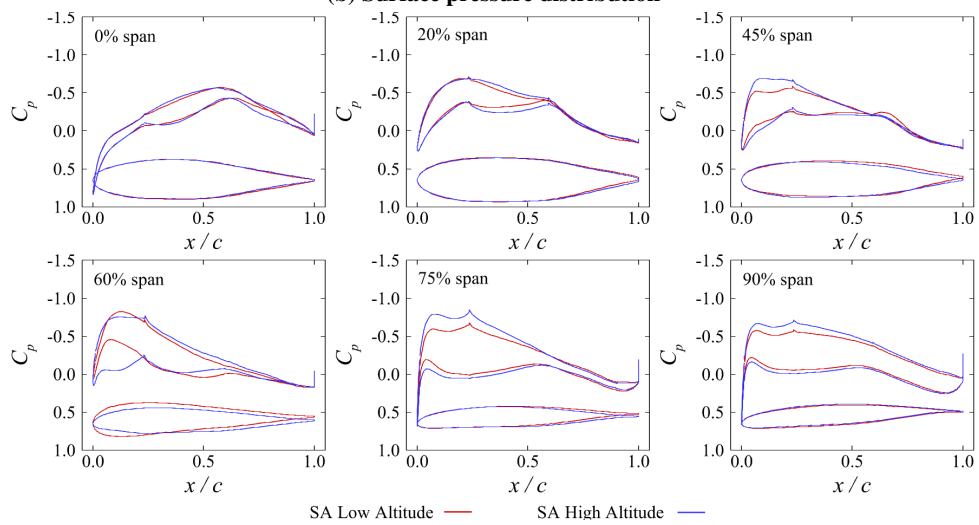
Flying-V aircraft cruise performance is maximized at altitudes above 13,000 m. While long-range aircraft can afford to climb to such high altitudes, stage lengths of single-aisle aircraft often limit their feasible cruise altitudes, highlighting the importance of efficiency at lower altitudes. This motivates the investigation of single-aisle-size Flying-V aircraft at different cruise altitudes. Comparing the solution information of the SA Low Altitude and SA High Altitude Flying V aircraft presented in Fig. 17, the majority of the difference in results can be attributed to the difference in cruise lift coefficient due to the lower ambient air density of SA High Altitude's flight level. The SA High Altitude has lower wing loading, with a 5% increase in planform area, to better balance the induced and viscous components of drag at the higher altitude. A notable feature of the single-aisle-size Flying-V aircraft is a total span less than the maximum allowable span for both aircraft, which suggests that an increase in inner-wing span reduces the wing loading too much to maintain efficiency at cruise. Increasing aspect ratio without adding significant planform area becomes difficult when the outer-wing planform is retained. The inner-wing sweep is seen to decrease for both cases similar to TA Planform Free. Both single-aisle-size cases deviate from the optimized twin-aisle-size geometry shown in grey in Fig. 8. The root chord is markedly larger, and the cabin-housing portion has a taper ratio that is further away from unity. The initial airfoil thickness was insufficient to wrap the cabin at the leading and trailing edges, prompting the extension of the root chord by the optimizer. For both aircraft, there is an appreciable thickness bulge at $y/b = 0.5$, which coincides with the end of the cargo cabin. Compared to the twin-aisle-size aircraft, both single-aisle-size designs have airfoils



(a) Spanwise lift distribution



(b) Surface pressure distribution



(c) Sectional pressure distributions

Fig. 17 Solution information for the single-aisle-size Flying-V aircraft.

Table 12 Performance of optimized single-aisle-size aircraft at the start of cruise.

Parameter	SA Low Altitude	SA High Altitude	A320neo
MTOW [kg]	70,800	68,800	78,000
Planform Area [m ²]	400	422	124
Span [m]	44.9	46.2	37.5
Inner-Wing Sweep [deg]	55	55	
AR _{wet} [-]	2.93	2.96	
Altitude [m]	10,973	13,411	
C_L [-]	0.160	0.216	
L/D [-]	20.2	23.2	
D	30,500	25,800	

with significantly higher thickness-to-chord ratios to accommodate the standard cabin height of 2.1 m, which is as an important design driver. The immediate thinning of the airfoils at the boundary between the passenger and cargo cabins (step change in height) further supports this claim. Despite the unusually thick airfoils, both single-aisle-size aircraft exhibit no significant shocks at a cruise Mach number of 0.78.

Table 12 summarizes the aerodynamic performance of the two single-aisle-size Flying-V aircraft. SA High Altitude performs significantly better, with a 16% reduction in drag and a 13% increase in lift-to-drag ratio. Both optimized designs have an inner-wing sweep of 55 degree and the planform areas of the optimized single-aisle-size Flying V aircraft are much larger than the A320neo. Despite that, the weight model produces a lower takeoff weight estimate for both Flying V aircraft, which can be attributed to the Flying-V configuration's assumed structural efficiency in the Delft weight model [24] and reduced fuel weight. Figure 18 highlights the aerodynamic performance of both aircraft across a range of lift-coefficients. In both cases, the nominal cruise lift coefficient is lower than the lift coefficient that maximizes lift-to-drag ratio, underscoring the benefit that a high cruise altitude brings for this aircraft configuration.

Aerodynamic Performance Impact of Variations in Passenger Cabin Height

Inspection of the geometries obtained for SA Low Altitude and SA High Altitude reveals the passenger cabin height to be a driving factor in the shaping of the aircraft OML. This section discusses a study performed to understand the efficiency benefit of reducing the passenger cabin height from 2.1 m to 1.9 m. When the aircraft are optimized with the reduced cabin height, the aircraft planform is shrunk in the chord-wise direction for both aircraft to reduce viscous drag. SA High Altitude trades off a fraction of the area reduction for an increase in span. Table 13 compares the key performance figures between the regular and reduced-height cabin aircraft. For both the SA Low Altitude and SA High Altitude, a 0.2 m reduction in cabin height results in approximately a 2% gain in lift-to-drag ratio. The weight implications of the reduction in planform area are not considered in this study to better highlight the aerodynamic influence of the cabin height.

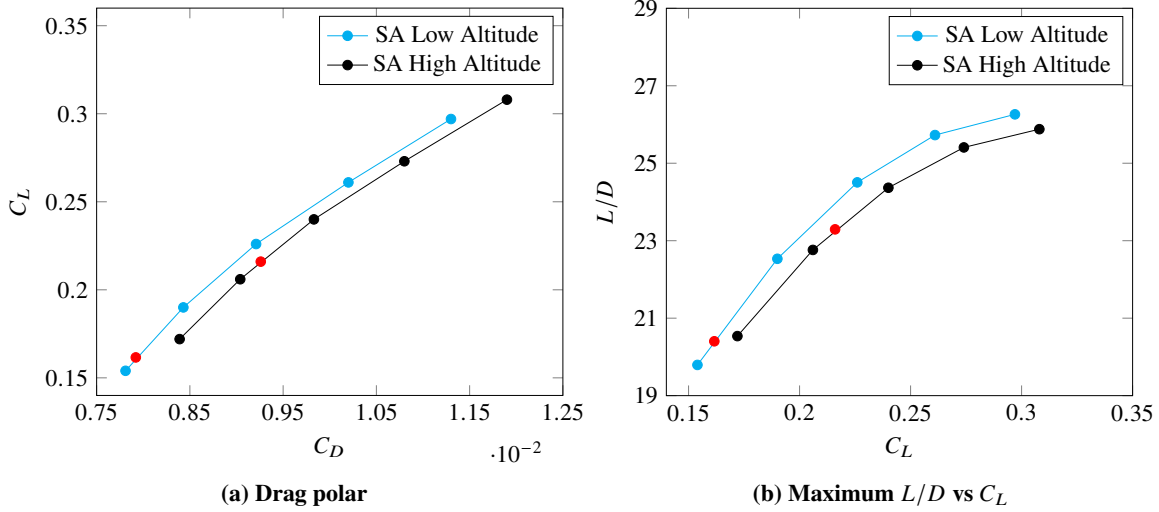


Fig. 18 Aerodynamic properties of the single-aisle-size Flying-V aircraft at low and high altitudes (Mach 0.78 at Reynolds numbers of 67 and 45 million, respectively). Red symbols represent optimization operating points.

Table 13 Aerodynamic performance comparison between full-height and reduced-height passenger cabin single-aisle-size Flying-V aircraft with fixed weight.

Design	Cabin Height [m]	Planform Area [m ²]	C_L [-]	C_D [-]	L/D [-]
SA Low Altitude	2.1	399.5	0.160	0.0079	20.2
	1.9	391.7	0.160	0.0078	20.6
SA High Altitude	2.1	421.5	0.216	0.0093	23.2
	1.9	412.0	0.216	0.0092	23.5

VII. Aerodynamic Performance Impact of Control-Surface Hinge Line

A control surface, especially when spanning a significant portion of the aircraft’s trailing edge, impinges on the optimizer’s ability to freely shape and twist that portion of the wing. A control-surface hinge line is defined based on van Luijk and Vos [12] and implemented in a side-study to quantify the performance penalty of its implementation across the transition region and outerwing of the Flying-V aircraft. The performance impact of the straight hinge line is seen to be small. Each of the four principal designs: TA Planform Fixed, TA Planform Free, SA Low Altitude, SA High Altitude, exhibit less than a 1% loss in performance when the constraint is included in the formulation of the optimization problem.

VIII. Effect of Grid Density on Optimization Results

Optimizations were performed at twice the nominal grid resolution to evaluate whether the default optimization grid (L0 grid: 1.7×10^6 nodes) captures the flow characteristics sufficiently to produce a design consistent with finer-grid optimizations. Fine-grid (L1 grid: 3.4×10^6 nodes) optimizations repeat the four principal optimization cases: TA Planform Fixed, TA Planform Free, SA Low Altitude, SA High Altitude. Performance figures obtained using Richardson

Table 14 Performance comparison of L0 and L1 grid-optimized aircraft.

Design	Altitude [m]	Mach [-]	C_L [-]	L0-Optimized		L1-Optimized	
				C_D [-]	L/D [-]	C_D [-]	L/D [-]
SA Low Altitude	10,973	0.78	0.160	0.0079	20.2	0.0076	20.4
SA High Altitude	13,411	0.78	0.216	0.0093	23.2	0.0092	23.3
TA Planform Fixed	13,000	0.85	0.262	0.0103	25.5	0.0104	25.1
TA Planform Free	13,000	0.85	0.234	0.0088	26.7	0.0087	26.9

extrapolation, as previously described, for designs optimized on the L0 and L1 grids are presented in Table 14. The difference in performance is within 1% for three of the four designs and 1.5% for the TA Planform Fixed case, which had the largest discrepancy. Overall, the results are comparable within the range of uncertainty associated with the analysis framework.

IX. Conclusions

The aerodynamic performance of the Flying-V aircraft configuration was investigated using RANS-based aerodynamic shape optimization in the twin-aisle and single-aisle classes. The initial aircraft geometry was chosen to match the planform developed by Faggiano et al. [8], which was then optimized to minimize drag subject to lift and trim constraints at the start-of-cruise operating point. Drag contributions associated with nacelles, pylons, and excrescences are not considered. Weight estimation for the optimized aircraft uses Torenbeek’s method for conventional components and fuel fractions and Bradley’s method for the non-cylindrical pressure vessel and inner-wing structure.

At the twin-aisle level, planform-fixed optimization with freedom in shape and twist subject to a cabin shape constraint, produces an aircraft with a lift-to-drag ratio of 25.5 at 13,000 m and a cruise static margin of 6%. The performance impact of static margin variations was studied using the preceding problem formulation, revealing a 4.4% increase in lift-to-drag ratio when reducing the margin from 9% to 2%, with 75% of the gain attained by relaxing the margin to 5%. Freedom in chord, span, and sweep angle enabled the optimizer to design an aircraft with a lift-to-drag ratio of 26.7, representing a 5% improvement. Despite a cruise Mach number of 0.85, the optimized Flying-V aircraft have only weak shocks and essentially zero wave drag. The planform-free optimization increased the aircraft’s span while reducing the chord and sweep, leading to a cabin layout of 3-2-3, which is narrower than the 3-4-3 layout of the baseline geometry. A two-point optimization case reveals that an 8% reduction in drag at a Mach number of 0.90 can be achieved for a 0.4% increase in drag at Mach 0.85.

Optimizations at the single-aisle size are performed with planform freedom. After selecting a 3-3 cabin layout based on exploratory optimizations, an appropriate optimization formulation was applied to single-aisle-size Flying-V aircraft flying at 10,973 m and 13,411 m with a cruise static margin of 6%. The high-altitude design has a lift-to-drag ratio of 23.2, while the low-altitude single-aisle-size Flying-V aircraft produced a lift-to-drag ratio of 20.2, again demonstrating

the Flying-V aircraft's affinity for flying at high altitude. This study is intended to investigate the aerodynamics of the configuration opposed to making aircraft-level claims about the competitiveness of the Flying V with present-day conventional designs. The inclusion of low-speed stability and control, field performance, higher-fidelity mass models, multi-mission design, and powerplant sizing in the problem formulation is recommended as a next step [19].

The primary conclusions of the present work are as follows:

- 1) Performance estimates based on RANS-based aerodynamic shape optimization corroborate the predictions of the Delft group [8].
- 2) RANS-based aerodynamic shape optimization produced geometries with very low wave drag and lift-to-drag ratios competitive with some of the best unconventional configurations.
- 3) The lift-to-drag ratio of the Flying-V aircraft can be further improved by reducing chord length and sweep angle while increasing span, but further study is needed that includes the impact on other disciplines.
- 4) The Flying-V concept can perform well in the single-aisle class, although its relative performance is more impressive in the twin-aisle class.

Funding Sources

This work was partially funded by the Natural Sciences and Engineering Research Council (NSERC), Transport Canada, and the University of Toronto Institute for Aerospace Studies.

Acknowledgments

Computations were performed on the Niagara supercomputer at the SciNet High Performance Computing (HPC) Consortium, which is a part of the Digital Research Alliance of Canada. The authors gratefully acknowledge the input and support provided by Aiden Gray.

References

- [1] Mithal, S., and Rutherford, D., "ICAO's 2050 net-zero CO₂ goal for International Aviation," *International Council on Clean Transportation*, 2023. URL <https://theicct.org/publication/global-aviation-icao-net-zero-goal-jan23/#:~:text=In%20October%202022%2C%20member%20states,emissions%20from%20aviation%20by%202050>.
- [2] Torenbeek, E., "Blended Wing Body and All-Wing Airliners," *European Workshop on Aircraft Design Education (EWADE)*, 2007.
- [3] R Martinez-Val and E Perez and J Puertas and J Roa, "Optimization of planform and cruise conditions of a transport flying wing," *Proceedings of the Institution of Mechanical Engineers, Part G: Journal of Aerospace Engineering*, Vol. 224, No. 12, 2010, pp. 1243–1251. <https://doi.org/10.1243/09544100JAERO812>.
- [4] Bravo-Mosquera, P. D., Catalano, F. M., and Zingg, D. W., "Unconventional aircraft for civil aviation: A review of

- concepts and design methodologies,” *Progress in Aerospace Sciences*, Vol. 131, Article 100813, 2022. <https://doi.org/https://doi.org/10.1016/j.paerosci.2022.100813>, URL <https://www.sciencedirect.com/science/article/pii/S0376042122000070>.
- [5] Blain, L., “Boeing to build braced-wing airliner, shooting for 30% efficiency gain,” , 01 2023. URL <https://newatlas.com/aircraft/boeing-nasa-truss-braced/>.
- [6] Blain, L., “JetZero aims to put ultra-efficient blended-wing jet in service by 2030,” , 05 2023. URL <https://newatlas.com/aircraft/jetzero-blended-wing/>.
- [7] Bolsunovsky, A., Buzoverya, N., Gurevich, B., Denisov, V., Dunaevsky, A., Shkadov, L., Sonin, O., Udzhuhu, A., and Zhurihin, J., “Flying wing—problems and decisions,” *Aircraft Design*, Vol. 4, No. 4, 2001, pp. 193–219. [https://doi.org/https://doi.org/10.1016/S1369-8869\(01\)00005-2](https://doi.org/https://doi.org/10.1016/S1369-8869(01)00005-2).
- [8] Faggiano, F., Vos, R., Baan, M., and Dijk, R., “Aerodynamic Design of a Flying V Aircraft,” AIAA Paper 2017-3589, 2017. <https://doi.org/10.2514/6.2017-3589>.
- [9] “B2 Spirit,” *US Air Force*, retrieved 5 February 2023. URL <https://www.af.mil/About-Us/Fact-Sheets/Display/Article/104482/b-2-spirit/>.
- [10] “Flying-V,” *TU Delft*, retrieved 10 October 2022. URL <https://www.tudelft.nl/lr/flying-v>.
- [11] Benad, J., “The Flying V - A New Aircraft Configuration for Commercial Passenger Transport,” 2015, pp. 1–8. <https://doi.org/10.25967/370094>, deutscher Luft- und Raumfahrtkongress 2015, Rostock ; Conference date: 22-09-2015 Through 24-09-2015.
- [12] van Luijk, N., and Vos, R., “Constrained Aerodynamic Shape Optimisation of the Flying V Outer Wing,” *AIAA AVIATION 2023 Forum*, American Institute of Aeronautics and Astronautics Inc. (AIAA), United States, 2023. <https://doi.org/https://doi.org/10.2514/6.2023-3250>.
- [13] Laar, Y., , Atherstone, D., and Vos, R., “Aerodynamic Design of a Flying V Aircraft in Transonic Conditions,” *AIAA SCITECH 2023 Forum*, American Institute of Aeronautics and Astronautics Inc. (AIAA), United States, 2024. <https://doi.org/https://doi.org/10.2514/6.2024-2669>.
- [14] Osusky, M., and Zingg, D. W., “Parallel Newton–Krylov–Schur Flow Solver for the Navier–Stokes Equations,” *AIAA Journal*, Vol. 51, No. 12, 2013, pp. 2833–2851. <https://doi.org/10.2514/1.J052487>.
- [15] Reist, T. A., Zingg, D. W., Rakowitz, M., Potter, G., and Banerjee, S., “Multifidelity Optimization of Hybrid Wing–Body Aircraft with Stability and Control Requirements,” *Journal of Aircraft*, Vol. 56, No. 2, 2019, pp. 442–456. <https://doi.org/10.2514/1.C034703>.
- [16] Chau, T., and Zingg, D. W., “Aerodynamic Optimization and Fuel Burn Evaluation of a Transonic Strut-Braced-Wing Single-Aisle Aircraft,” *Journal of Aircraft*, 2023, pp. 1–21. <https://doi.org/10.2514/1.C037158>, URL <https://doi.org/10.2514/1.C037158>.

- [17] Yazdi, R. R., Reist, T., and Zingg, D. W., “Aerodynamic Optimization of a Flying V Aircraft Based on the Reynolds-Averaged Navier-Stokes Equations,” AIAA Paper 2024-1909, January 2024. <https://doi.org/10.2514/6.2024-1909>.
- [18] Graver, B., Rutherford, D., and Zheng, S., “CO2 Emissions from Commercial Aviation: 2013, 2018, and 2019,” *The International Council on Clean Transportation*, 2020. URL <https://theicct.org/publication/co2-emissions-from-commercial-aviation-2013-2018-and-2019/>.
- [19] Gray, A. L., and Zingg, D. W., “Blended-Wing-Body Regional Aircraft Optimization with High-Fidelity Aerodynamics and Critical Design Requirements,” *Journal of Aircraft*, Vol. 61, No. 6, 2024, pp. 1775–1792. <https://doi.org/10.2514/1.C037876>, URL <https://doi.org/10.2514/1.C037876>.
- [20] Gagnon, H., and Zingg, D. W., *Geometry Generation of Complex Unconventional Aircraft with Application to High-Fidelity Aerodynamic Shape Optimization*, AIAA Paper 2013-2850, 2013. <https://doi.org/10.2514/6.2013-2850>.
- [21] Selig, M. S., “Airfoil Coordinate Database by Michael S. Selig,” , retrieved 10 October 2022. URL https://m-selig.ae.illinois.edu/ads/coord_database.html.
- [22] “Aircraft Container Sizes,” *Active Freight*, retrieved 20 January 2023. URL <https://www.activfreight.com.au/customer-resources/aircraft-container-sizes/>.
- [23] Torenbeek, E., *Synthesis of Subsonic Airplane Design: An Introduction to the Preliminary Design of Subsonic General Aviation and Transport Aircraft, with Emphasis on Layout, Aerodynamic Design, Propulsion and Performance*, Springer Netherlands, 1982.
- [24] Oosterom, W., and Vos, R., *Conceptual Design of a Flying-V Aircraft Family*, AIAA AVIATION 2022-3200, 2022. <https://doi.org/10.2514/6.2022-3200>, URL <https://arc.aiaa.org/doi/abs/10.2514/6.2022-3200>.
- [25] Reist, T. A., “Scaling of Hybrid Wing-Body-Type Aircraft: Exploration Through High-Fidelity Aerodynamic Shape Optimization,” Ph.D. thesis, University of Toronto, Toronto, ON, Nov. 2016.
- [26] “A320/21,” *ANA Cargo*, retrieved 11 March 2023. URL <https://www.anacargo.jp/en/int/specification/a320.html>.
- [27] Hicken, J. E., and Zingg, D. W., “Aerodynamic Optimization Algorithm with Integrated Geometry Parameterization and Mesh Movement,” *AIAA Journal*, Vol. 48, No. 2, 2010, pp. 400–413. <https://doi.org/10.2514/1.44033>, URL <https://doi.org/10.2514/1.44033>.
- [28] Osusky, L., Buckley, H., Reist, T., and Zingg, D., “Drag Minimization Based on the Navier–Stokes Equations Using a Newton–Krylov Approach,” *AIAA Journal*, Vol. 53, 2015, pp. 1555–1577. <https://doi.org/10.2514/1.J053457>.
- [29] Sederberg, T. W., and Parry, S. R., “Free-form deformation of solid geometric models,” Vol. 20, No. 4, 1986, p. 151–160. <https://doi.org/10.1145/15886.15903>, URL <https://doi.org/10.1145/15886.15903>.
- [30] Gagnon, H., and Zingg, D., “Two-Level Free-Form and Axial Deformation for Exploratory Aerodynamic Shape Optimization,” *AIAA Journal*, Vol. 53, 2015, pp. 1–12. <https://doi.org/10.2514/1.J053575>.

- [31] Gill, P. E., Murray, W., and Saunders, M. A., “SNOPT: An SQP Algorithm for Large-Scale Constrained Optimization,” *SIAM Journal on Optimization*, Vol. 12, No. 4, 2002, pp. 979–1006. <https://doi.org/10.1137/S1052623499350013>.
- [32] Zingg, D. W., Nemec, M., and Pulliam, T. H., “A Comparative Evaluation of Genetic and Gradient-Based Algorithms Applied to Aerodynamic Optimization, journal = European Journal of Computational Mechanics,” Vol. 17, No. 1-2, 2008, pp. 103–126. <https://doi.org/10.3166/remn.17.103-126>, URL <https://doi.org/10.3166/remn.17.103-126>.
- [33] Chernukhin, O., and Zingg, D. W., “Multimodality and Global Optimization in Aerodynamic Design,” *AIAA Journal*, Vol. 51, No. 6, 2013, pp. 1342–1354. <https://doi.org/10.2514/1.J051835>, URL <https://doi.org/10.2514/1.J051835>.
- [34] Hicken, J. E., and Zingg, D. W., “A Simplified and Flexible Variant of GCROT for Solving Nonsymmetric Linear Systems,” *SIAM Journal on Scientific Computing*, Vol. 32, No. 3, 2010, pp. 1672–1694. <https://doi.org/10.1137/090754674>, URL <https://doi.org/10.1137/090754674>.
- [35] Reist, T. A., and Zingg, D. W., “High-Fidelity Aerodynamic Shape Optimization of a Lifting-Fuselage Concept for Regional Aircraft,” *Journal of Aircraft*, Vol. 54, No. 3, 2017, pp. 1085–1097. <https://doi.org/10.2514/1.C033798>.
- [36] Reist, T. A., Koo, D., Zingg, D. W., Bochud, P., Castonguay, P., and Leblond, D., “Cross Validation of Aerodynamic Shape Optimization Methodologies for Aircraft Wing-Body Optimization,” *AIAA Journal*, Vol. 58, No. 6, 2020, pp. 2581–2595. <https://doi.org/10.2514/1.J059091>, URL <https://doi.org/10.2514/1.J059091>.
- [37] Reist, T. A., Koo, D., and Zingg, D. W., “Aircraft Cruise Drag Reduction Through Variable Camber Using Existing Control Surfaces,” *Journal of Aircraft*, Vol. 59, No. 6, 2022, pp. 1406–1415. <https://doi.org/10.2514/1.C036754>, URL <https://doi.org/10.2514/1.C036754>.